Tailoring Polyelectrolyte Multilayer Nanofiltration Membranes by Aerosol-assisted Printing: Insights into Membrane Formation Mechanisms

Lihong Gan,[†] Jin Zhang,[†] Yangtao Wu,[†] Zhuo Chen,[†] Zhenyu Zhao,[†] Shihong Lin,[§] and Yi Jiang*[,†]

[†]Department of Civil and Environmental Engineering, The Hong Kong Polytechnic University, Kowloon, Hong Kong, China

[§]Department of Civil and Environmental Engineering and Department of Chemical and Biomolecular Engineering, Vanderbilt University, Nashville, Tennessee 37235-1831, United States

* To whom correspondence should be addressed:

Yi Jiang: Tel: +852-27666044; Fax: +852-23346389; Email: yi-cee.jiang@polyu.edu.hk

Abstract

Polyelectrolyte multilayer (PEM) membranes, with advantageous features of versatile chemistry and structures, are driving the development of advanced nanofiltration (NF) membranes with exceptional performance. While developing a printing method holds great promise for the eventual mass production of these membranes, reports on the printing method and the underlying mechanisms of membrane formation are currently scarce. Herein, we develop an aerosol-assisted printing (AAP) system for fabricating PEM NF membranes with highly tunable separation characteristics. Our study unveils the three stages of membrane formation from assembly of polyethyleneimine (PEI) and poly (sodium 4-styrenesulfonate) (PSS): aerosol deposition, single PE layer formation, and PEM assembly. The droplet deposition is governed by inertial impaction, and the deposited PE migrate/entangle to form a single PE layer. The thicknesses of the PE layer and PEM exhibits linear growth as the number of printing scan increases. Furthermore, PE interdigitation forms an effective polymeric network barrier, which increases resistance to solute and water transport. By manipulating the PE deposition mass and layering, PEM membranes with tunable pore radii (0.40-0.56 nm) and water permeability (5-60 $L \cdot m^{-2} \cdot h^{-1} \cdot bar^{-1}$) were obtained for various water treatment applications, ranging from micropollutant removal to humic acid filtration. Our study offers valuable mechanistic insights into the PEM formation and precise structural adjustment via printing, thus facilitating scalable manufacturing and widespread applications of the PEM NF membranes.

Keywords: polyelectrolyte multilayer, nanofiltration, aerosol, printing, polyelectrolyte complex.

Table of Contents Graphic

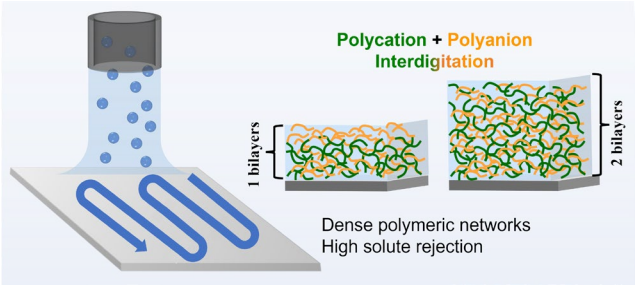

Synopsis

We have invented an aerosol-assisted printing method for producing highly customizable polyelectrolyte multilayer nanofiltration membranes that offers significant advantages over the conventional dip coating process.

Introduction

Nanofiltration (NF) is an attractive pressure-driven membrane process for advanced water treatment because it can remove all pathogens and most organic and inorganic contaminants in a single treatment step. Polyelectrolyte multilayer (PEM) membranes represent a distinct category of NF membranes as compared to commercial polyamide-based membranes, featuring a selective layer composed of alternatively charged polyelectrolytes (PEs) assembled in a layer-by-layer (LbL) fashion. PEM membranes are attractive because of their versatile chemistry and structures, which enable the creation of advanced NF membranes with excellent permselectivity (e.g., divalent over monovalent cations,[1] organic contaminant over cations[2, 3]), chemical stability (e.g., much higher chlorine or acid/base resistance than polyamide membranes[4-6]), and fouling resistance.[7-10] These distinctive features offer new possibilities for chemical separations that are challenging for conventional polyamide membranes.

The past two decades have witnessed a keen interest in developing and applying PEM membranes in water treatment. However, despite numerous research with regard to their principles and applications, there has not been a viable technical route for those membranes to be made at an industrial scale and with easiness in controlling their fabrication and structure at a large manufacturing scale. The current method to assemble PEM is dip coating, which cycles a substrate between two reservoirs containing aqueous solutions of PEs of opposite charges. In dip coating-based LbL deposition, a layer of PE adds to the oppositely charged substrate or the previously deposited layer via electrostatic force. The method usually takes a few hours to several days to achieve enough bilayers due to the diffusive time scale.[11] As a result, it is almost impossible for the dip coating method to be scaled up for high-throughput using roll-to-roll fabrication. Also, the

dip coating method requires a large reservoir of PE for immersion, which results in a significant waste of chemicals.

A printing method that utilizes the spray of PE droplets holds great promise for the mass production of PEM. Due to the improved means of mass transfer, the membrane preparation time can be drastically decreased and much smaller solution quantity can be used.[12, 13] Schlenoff et al.[14] have suggested that the morphology, uniformity, and chemical composition of sprayed PEM, as well as the selective membrane properties, are virtually identical to those prepared by dip coating. In 2014, Kentish et al. demonstrated an NF membrane via spray coating of an active layer of poly(acrylic acid) (PAA) and poly(allylamine) hydrochloride (PAH).[15] The membrane can reject up to 80% $CaCl_2$ and 50% NaCl, with a water flux of 1.1-2.3 L m^{-2} h^{-1} bar^{-1}. The spray technique was further used to deposit an ultrathin (ca. 70 nm) active layer consisting of PAH and poly(sodium 4-styrenesulfonate) (PSS), which showed 94% rejection of NaCl with a permeate flux of 0.75 L m^{-2} h^{-1} bar^{-1}.[16]

Despite these early demonstrations, there remain critical knowledge gaps in how a PEM membrane forms during printing. The membrane printing process is complex and involves droplet deposition (aerosolization, transport, impingement, and possible resuspension of droplets), building block assembly, and subsequent evolution into a hierarchical structure.[17] One notable influencing factor is the droplet size. Previous studies on spray/droplet-based PEM membrane preparation have primarily involved the use of a spray gun in a fixed position, and the droplets examined in these studies are typically large, ranging from 30 to 50 μm in size. This size limitation hampers the ability to finely tune the membrane structure, including its thickness and pore size. Large droplets result in a high mass deposition on the substrate over a very short time (a few seconds), consequently leading to the formation of thick PE layers.[18] As a result, the dense nature

of the deposited layers leads to a low water permeability. Moreover, the drying of these large droplets causes uneven distribution of PEs over the substrate, inducing poor homogeneity and high surface roughness, primarily due to the coffee-ring effect.[19, 20] Droplet velocity is another factor that could have an influence on the kinetic energy of the droplets and thus the impingement of the droplets on the membrane surface. Finally, there remains no information on how the deposited PE molecules assemble into a layer and subsequently a PEM. This is primarily due to a lack of essential experimental data on the deposition of the droplets. Therefore, achieving precise control over droplet generation and deposition becomes critical to finely tuning the membrane's structure and separation properties.

In this study, we develop an aerosol-assisted printing (AAP) system by modifying a commercial 3D printer with a Collison nebulizer. The Collison nebulizer, a well-established aerosol generation instrument known for its high reproducibility and wide range of applications, is selected as the standard droplet generation setup.[21-24] The produced aerosols are water droplets with a narrow and small size distribution (mainly 3-5 μm). This choice enables us to not only delicately control the PEM structure and property, but also conveniently construct a conceptual model of the membrane formation. Additionally, we demonstrate the printing of PEM membranes with a large area of 160 cm^2 with a 3D printer. The printing process involves the use of polyethyleneimine (PEI) as the polycation and poly(sodium 4-styrenesulfonate) (PSS) as the polyanion. The deposition of the PE aerosols is characterized using a suite of state-of-the-art in-line techniques, including laser diffraction size analyzer (LDSA), laser doppler velocimetry (LDV), and is modeled by COMSOL simulation. These characterization and modeling provide new information on the droplet size and velocity for understanding the membrane formation (i.e., the growth of the PEM). By changing the printing process parameters, including per-layer scan number and bilayer number, a spectrum

of membrane separation performance, spanning from loose to dense nanofiltration, is achieved. Consequently, our study presents novel mechanistic insights into the formation and precise adjustment of a PEM selective layer using the printing method. This significant contribution expands the current understanding of PEM membrane fabrication techniques, opening up new avenues for advancements in the field.

Materials and Methods

Materials and Chemicals. A polyacrylonitrile (PAN) membrane (PX, Sterlitech) with a nominal molecular weight cut off (MWCO) of 400 kDa was used as the substrate. PEI (MW 750 kDa, Sigma-Aldrich) and PSS (MW 1000 kDa, Sigma-Aldrich) were used as the polycation and polyanion respectively. A commercial NF membrane (NF270, Dow-Filmtec) was used as a reference membrane for performance comparison. NaOH was purchased from Unichem and Na_2SO_4 was from J&K Scientific. Humic acid (HA), $MgSO_4$, $MgCl_2$, and NaCl were purchased from Sigma-Aldrich. Erythritol, xylose, glucose, and sucrose (Aladdin) were used as the reference organic solutes to evaluate the dependence of rejection on solute size. Bisphenol A (BPA, J&K Scientific), antipyrine (AP, Sigma-Aldrich), ofloxacin (OFX, Sigma-Aldrich), and ciprofloxacin (CIP, Sigma-Aldrich) were selected micropollutants to test the rejection performance of prepared membranes. Pure water (Milli-Q plus system, Millipore) was used for preparing solutions and testing membrane water permeability.

Aerosol-assisted Printing (AAP) Setup. The AAP setup was constructed in our laboratory as illustrated in Figure S1. The equipment consists of an aerosol spray system, a pressure supply system, and a 3D printer. The aerosol spray system includes two six-jet Collison nebulizers (CH

Technologies). The PE solutions (8.0 g L^{-1} PEI or 16.0 g L^{-1} PSS in water) were separately added to the two nebulizer jars. The Collison nebulizer produces micrometer-sized (mainly from 3 to 5 μm) aerosols/droplets.[22] A stainless-steel tube as the nebulizer outlet (diameter 14 mm) was aligned perpendicular to the platform/substrate surface. The distance between the nozzle and the membrane substrate surface was 15 mm. The pressure supply system provides a constant pressure of 0.5-1.5 bar by an air compressor. The 3D printer (3DLDL, six point zero inc.) was used to control the movement of the nozzle. The nozzle moved at a speed of 1,500 mm min^{-1} in a raster scan pattern, with a 7 mm line spacing (Figure S2). It takes ca. 1.5 min to print one scan of PE on a substrate with an effective area of 64.8 cm^2. Further details on the AAP method are given in Text S1.

PEM Membrane Fabrication. The PAN substrate was soaked in ethanol and rinsed with pure water to remove the preservatives. Afterwards, the PAN substrate was hydrolyzed in a 2.0 M NaOH solution at ambient temperature for 2 h. After removing excessive NaOH by rinsing the substrate with pure water, the hydrolyzed PAN (HPAN) substrate was kept in pure water for further PEM membrane preparation. The schematic of membrane printing is shown in Figure 1a, and the PEM membrane formation is further schemed in Figure 1b. The complete movement of the nozzle over the entire substrate area was denoted as one scan, and 1-5 scans were conducted to form a single layer with different deposition masses. More printing scans result in more deposited PE mass for a single PE layer. The resultant layer was denoted as PEI_n or PSS_n (n represents scans, n=1-5). A PE bilayer was formed by cycling deposition of the positively charged PEI and negatively charged PSS layers. The resultant membrane with one bilayer was denoted as $(PEI_nPSS_n)_1$. For example, $(PEI_3PSS_3)_1$ indicates the membrane with one PEI/PSS bilayer whose terminating layer is PSS, and both the PEI and PSS layers were printed with three scans of the PE

159 deposition. A series of PEM membranes were prepared with varied scans (1-5) and bilayer
160 numbers (1-2).

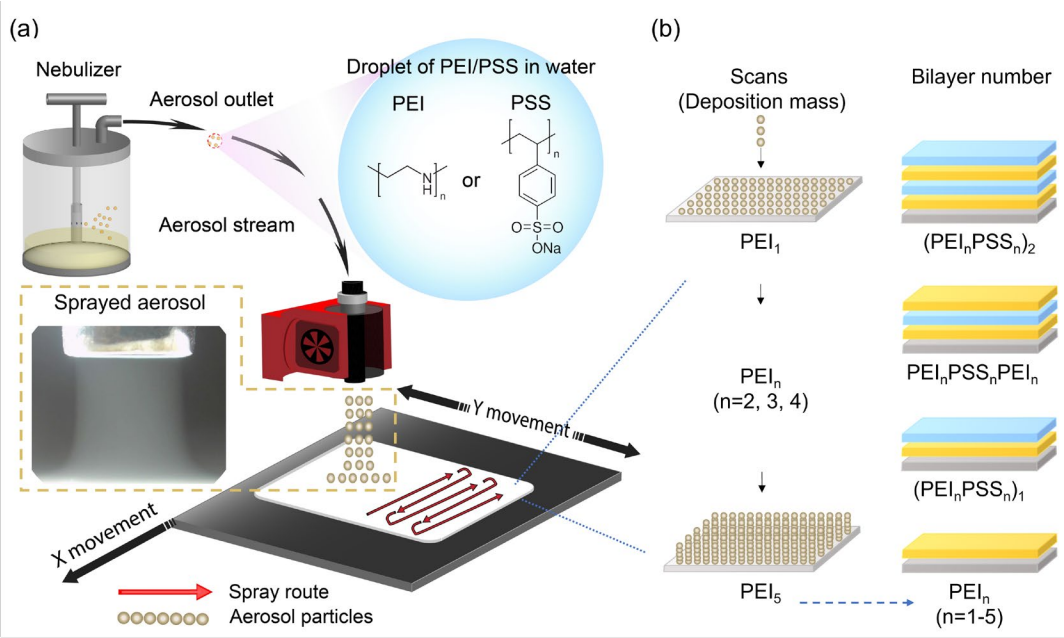

161

162 **Figure 1**. Schematics of (a) the PEM membrane fabrication process via aerosol-assisted printing
163 and (b) formation of the $(PEI_nPSS_n)_x$ membrane with various scans and bilayer numbers. Note: n
164 represents n scans for each PEI or PSS layer (n =1-5).

165 **Characterization of Aerosol Deposition Process.** Advanced in-line and off-line characterization
166 and modeling techniques were used to analyze the aerosol/PE deposition process. The velocity
167 field of the aerosol flow was monitored by a 2D mini laser Doppler velocimeter (LDV,
168 Measurement Science) as detailed in Text S2. A schematic diagram of the measurement positions
169 of the Collison nebulizer is shown in Figure S3a. A laser diffraction size analyzer (Winner 311XP,
170 Jinan Winner) was used to determine the size distribution of droplets produced by the Collison
171 nebulizer. To obtain the size distribution and microscopic morphology of the deposited, dried PE
172 particles, a trace amount of the PE was deposited on a silicon surface for atomic force microscopy

(AFM, Bruker NanoScope 8, Bruke) or on a transmission electron microscope (TEM) grid for TEM (JEM-2010, JEOL) analysis, respectively. The dried PE particle size distribution was analyzed from the AFM phase images using the Image J software. Deposition efficiency was determined as the ratio of the PE mass deposited over that delivered out of the nebulizer.

COMSOL Simulation. The fluid flow and mass transport processes were simulated utilizing COMSOL Multiphysics version 6.1. A two-dimensional axisymmetric model was developed to simulate the aerosol flow out of the spray nozzle. This model replicates the spatial configuration of the actual spray setup, focusing on a 2D region measuring 60 mm in length and 15 mm in height, which bisects the aerosol flow along its central axis and is oriented vertically to the membrane substrate. The velocity distribution obtained by LDV (Figure S3) was employed as the velocity boundary condition for the computational fluid dynamics (CFD) simulation. For the turbulence calculation, the k-ε model within the Reynolds-Averaged Navier-Stokes (RANS) framework was utilized to simulate the velocity distribution of the airflow field. The environmental conditions for the CFD simulation were set to a temperature of 293.15 K and an atmospheric pressure of 101.325 kPa.

Membrane Characterization. The membrane coupons were air-dried at ambient temperature before characterization. Attenuated total reflection Fourier transform infrared spectroscopy (ATR-FTIR, PerkinElmer Spectrum Two) was used to investigate the surface chemistry evolution during the PEM assembly, with a resolution of 4 cm^{-1} and a wavenumber range from 4,000 to 400 cm^{-1}. Membrane surface zeta potential was measured using a streaming potential analyzer (SurPASS electrokinetic analyzer, Anton Paar) with 1 mM KCl solution as the background electrolyte. The distribution of deposited PEI and PSS on the membrane surface was characterized using Raman mapping (inVia Micro-Raman microscope, Renishaw). A laser with a 785 nm wavelength was

used as the excitation source. Surface and cross-sectional images of the PEM membranes were obtained using the field emission scanning electron microscope (FESEM, Tescan MAIA3) after sputter coating the samples with gold (MCM-200 ion sputter coater, Micro Optics), and the PEM thickness was measured from these images using ImageJ. Membrane surface roughness was evaluated by using AFM in a tapping mode. The X-ray photoelectron spectroscopy (XPS, Nexsa G2 surface analysis system, Thermo Fisher Scientific) combined with depth profiling was used to obtain a detailed chemical analysis of PEM membranes. Detailed XPS information can be found in Text S3.

Membrane Filtration Performance Evaluation. Membrane filtration performance was evaluated using a crossflow filtration setup (FlowMEM-0021-HP, FMT). Each membrane coupon, having an effective area of 64.8 cm^2, was tested at 5 bar and a crossflow velocity of 38.5 cm s^{-1}. The membrane was compacted by pure water under a pressure of 5 bar for 2 hours before collecting data for separation performance. The weight of the permeate was measured using an automatic electronic balance (Ohaus, SPX2201) at a 60 s interval for 30 min.

The MWCO values of the membranes were determined by fitting the intrinsic rejection curve of neutral sugars of various molecular weights (erythritol 122 Da, xylose 150 Da, glucose 180 Da, sucrose 342 Da). The concentrations of the solutes were measured using a total organic carbon (TOC) analyzer (TOC-L, Shimadzu, Japan). The feed solution of each sugar was 50 mg TOC L^{-1}. To account for the concentration polarization effect, mass transfer coefficients were obtained based on fitting the experimental data and used to obtain the intrinsic rejection (Text S4).[25] The average pore sizes of the PEM membranes with different scans and bilayer numbers were estimated from the steric hindrance pore model (Text S5) using intrinsic rejections of the reference organic solutes mentioned above.[26, 27] Rejection of micropollutants including BPA, AP, OFX, and CIP was tested

using feed solutions containing 0.5 mg L^{-1} of each micropollutant, and their concentrations were measured using high-performance liquid chromatography (HPLC) as detailed in Text S3.

Results and Discussion

Polyelectrolyte Aerosol Generation, Characterization, and Deposition

***Polyelectrolyte Droplet Generation by Aerosolization*.** The aerosolization was accomplished by the Collison nebulizer where the liquid was broken up into droplets by high-speed gas flow. The size distribution of water droplets was mainly in the range of 3-5 μm with a volumetric median diameter (D_{v50}) of ca. 3.8 μm (Figure S4), which is consistent with our previous study.[22] The ultrafine droplets sprayed by the current system, due to their faster evaporation, can effectively hinder PE aggregation at the droplet edge[28] and promote even distribution on the surface. The aerosol diameter can be adjusted by applying varied nebulizer pressures (Figure 2a, b). With an increase of nebulizer pressure from 0.5 to 1.5 bar, the D_{v50} of PEI droplets decreased from 3.6 to 2.4 μm and the D_{v50} of PSS droplets decreased from 3.1 to 2.3 μm (Figure 2c). The D_{v50} of PEI droplets was larger than that of PSS droplets generated at the same nebulizer pressure due to the different viscosities of their solutions (5 and 20 mPa·s, respectively). Higher viscosity increases liquid retention in the nebulizer transfer channel, while the reduced channel diameter boosts gas velocity, leading to finer atomization of the liquid stream into smaller droplets compared to low-viscosity liquids.[29]

PE Aerosol Transport. The 2D vertical velocity distribution field of the aerosol flow from the nozzle to the substrate as measured by LDV is shown in Figure S3b-f. The velocity field exhibited a trend where the maximum velocity was initially attained at the nozzle exit, followed by a deceleration caused by air drag.[30] Under the operating pressure of 1 bar, the droplet velocity at the nozzle exit was ca. 1.1 m s^{-1}, and the velocity of aerosols reduced to ca. 0.6 m s^{-1} at 5 mm from the substrate (i.e., the lowest height that can be measured by the LDV due to limited laser angle).

As the operated pressure increased from 0.5 to 1.5 bar, the velocity at the nozzle exits increased from 0.7 to 1.3 m s^{-1} (Figure 2d).

To enable a more in-depth analysis of aerosol transport, COMSOL software was used to simulate the velocity field that was not detected by LDV. In the simulated velocity field, the vertically downward airflow started to form an abrupt bend in the streamlines. This bending stream encountered the substrate again, causing it to change direction and bend upwards (Figure 2e). As shown in Figure S5, the velocity of upward airflow under nebulizer pressure of 1.5 bar was ca. 1.0 m/s at the coordinates (x = ±25 mm, z = 7 mm). This velocity was notably higher than the velocity under 1.0 bar (ca 0.6 m/s), as shown in Figure 2e. In general, increasing nebulizer pressure increased both downward and upward aerosol velocities.

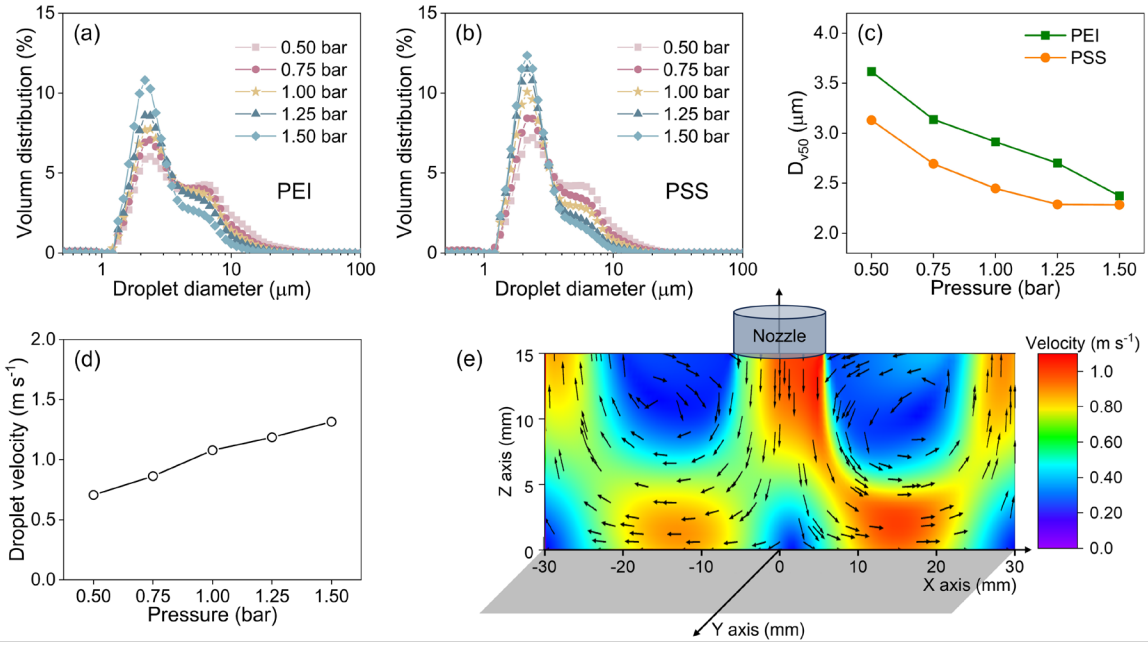

Figure 2. Droplet and particle size measurement: size distribution of (a) PEI and (b) PSS droplets generated under different nebulizer pressure; (c) the D_{v50} of PEI and PSS droplets under different nebulizer pressure; (d) droplet velocity of PEI aerosols at the nozzle exit under different nebulizer

pressure; (e) velocity distribution field under 1 bar nebulizer pressure from the COMSOL simulation.

Aerosol Deposition Mechanism. The effluent stream of PE aerosols was directed towards a flat membrane surface, causing the flow to deflect and creating a curvilinear flow shape (Figure 2e). Curvilinear motion is characterized by a dimensionless number called *Stokes number* (S_{tk}),[31] which is an indicator of a droplet's tendency to deposit on a surface.[32] A droplet with a low S_{tk} follows the fluid streamlines, while a particle with a larger S_{tk} can be dominated by its inertia and continues along its initial trajectory.

$$S_{tk} = \frac{\rho_P {d_P}^2 V}{18\mu L} \quad (1)$$

where d_p, ρ_P, and V are the droplet diameter, density, and velocity, respectively, μ is the dynamic viscosity of the carrier gas, and L is the characteristic length (jet diameter).

Based on the S_{tk} (Eq. 1), the aerosol size and velocity are the two main factors affecting the inertial deposition efficiency. Increasing PEI droplet velocity at the nozzle exits from 0.7 to 1.3 m s^{-1} (Figure 2d) could promote its deposition from 6.6% to 12.0% (Figure S6a). Furthermore, due to the larger size and consequent greater momentum, PEI droplets exhibited a 12.0% deposition efficiency compared to 1.2% for PSS droplets (Figure S6b).

We then estimated the diameter of a (completely dried) PE particle from a droplet by the one-droplet-one-particle (ODOP) principle based on mass conservation.[22, 33, 34]

$$D_p = D_d (C/\rho)^{1/3} \quad (2)$$

where D_d and D_p are the diameters of the droplet from the nebulizer and the dried particle, respectively, C is the concentration of the precursor PE solution, and ρ is the density of that PE.

277 Based on Eq. 2, a 2.9 μm PEI droplet corresponds to a PEI particle diameter of 574 nm, while
278 a 2.4 μm PSS droplet corresponds to a PSS particle diameter of 651 nm. We then measured the
279 sizes of the deposited PE particles by AFM (Figure 3b) and TEM (Figure S7). The AFM analysis
280 shows the PEI particles have a peak diameter of ca.14 nm, and the deposited PSS particles have a
281 peak diameter of ca. 12 nm. Obviously, the measured sizes from AFM (also those estimated from
282 the TEM images) were smaller than the calculated sizes from the ODOP principle, suggesting that
283 the droplets do not evaporate completely when they reach the substrate. Instead, the droplets spread
284 upon their impaction on the substrate, leading to the distribution of the PE over the surface, thereby
285 forming smaller PE particles.
286
287 **Membrane Formation Mechanism**
288 ***Formation of a PE Layer***. Based on the above aerosol deposition analysis, we prepared PEM
289 membranes under the optimal condition of maximum deposition efficiency (i.e., 1 bar). By
290 continuous spraying, more PEs were deposited over the substrate, leading to the gradual formation
291 of a PE layer (Figure 3a). We measured the growth kinetics of the PE layer with scan numbers by
292 analyzing the corresponding cross-sectional SEM images (Figure S8). As the scan number
293 increased, the deposited PE amount also increased, resulting in a proportional increase in the
294 thickness of the PE layer (Figure 3c). To better understand the PE layer structure, two conceptual
295 structural models were established, as schemed in Text S6. The first model is a solid film made of
296 PEs (solid film model), devoid of any porosity; the other model is a film of orderly packed PE
297 spheres (packed sphere model), with a theoretical void space of 48% (Figure S9). The calculated
298 thickness of the PEI_3 layer in the solid film and packed sphere models were 98 nm and 188 nm,
299 respectively; and the thickness of the PSS_3 layer in the solid film and packed sphere models were

56 nm and 107 nm, respectively (Table S1). The thicknesses of the PEI_3 and PSS_3 layers were measured to be 109 ± 26 nm and 96 ± 17 nm, respectively, from the SEM images (Figure S8), falling within the range between those of the solid film and packed sphere models. Based on the conceptual models, the actual PE layer structure is tightly packed. After impingement, the droplets spread, and the deposited PE within the droplets undergo migration due to diffusion and/or electrostatic attraction.[35] They eventually assemble into a thin film.[17] Moreover, the growth of the PEI or PSS layer followed a linear pattern (Figure 3c, $R^2 = 0.96$-0.99), with a rate of ca. 44 nm/scan, suggesting uniform intermolecular interactions along the depth of the layer. Porcel et al [36] have also reported that the layer thickness increases linearly with the spraying time. Although the PEM may shrink in thickness due to water removal under the vacuum condition for SEM, the linear increase trend in thickness matches the ellipsometry measurements in air.[37, 38]

Another interesting observation is that the printing mode by moving the nozzle resulted in even deposition of PEs. To visualize the difference, we deposited polyethylene blue dyes on the substrate in both fixed and moving nozzle modes. There was an uneven deposition of dyes under the fixed nozzle mode, showing a ring-shaped pattern (Figure S10a), with more deposition on the right side than on the left side. This result is consistent with the simulation result (Figure 2e), which shows that the higher velocity on the right side leads to increased momentum and, consequently, more significant deposition in that area. This non-uniform distribution of momentum is due to the bending of the spray tube. In the printing mode, however, the center of the nozzle passed over the entire substrate, resulting in even deposition of droplets (Figure S10b).

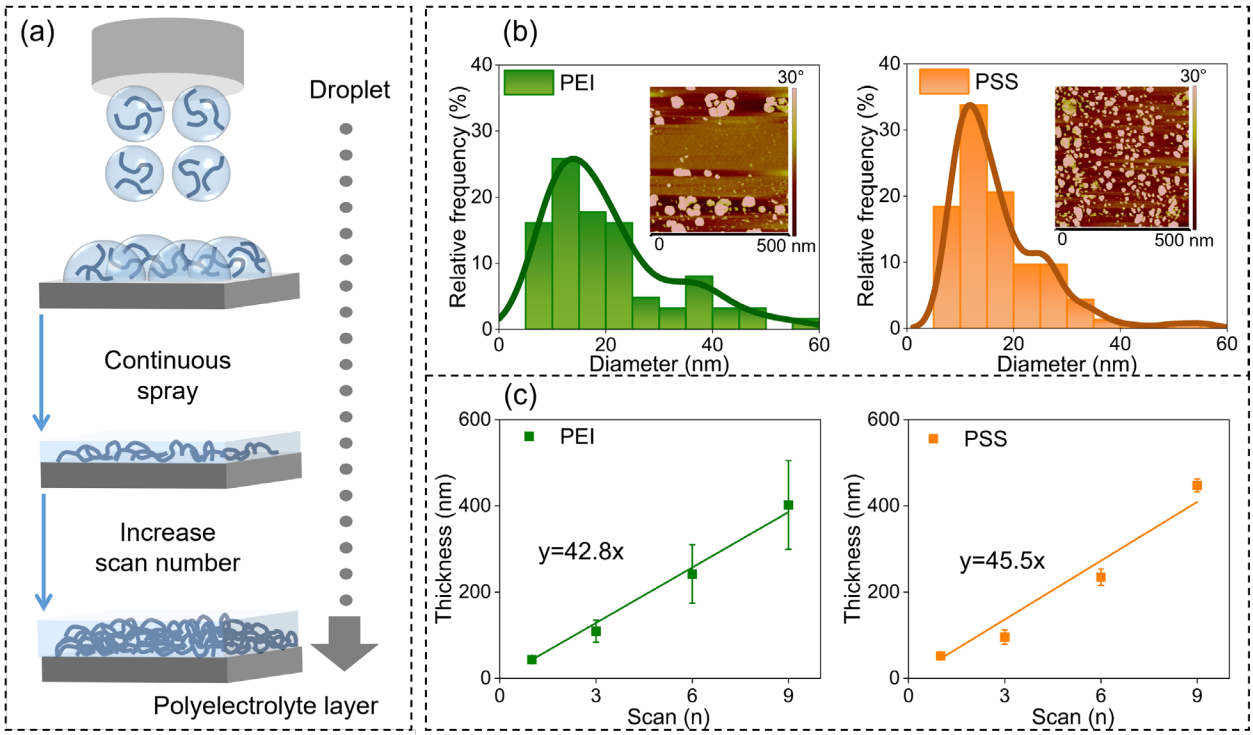

Figure 3. (a) Schematic of a PE layer formation showcasing the transformation from droplets into a complete PE layer; (b) size distribution of deposited PEI and PSS particles on the silicon wafer, and the inset figures are representative phase AFM images; (c) variation in the thickness of the PEI and PSS layers with different scans obtained from analysis of cross-sectional SEM images.

PEM Assembly. The PEM assembly was monitored by ATR-FTIR (Figure 4a). The peak at approximately 1690 cm^{-1} corresponds to the C=O bond in the COO^- group, which results from the hydrolysis of the C≡N groups under alkaline conditions.[39] This characteristic peak became less intensive when the amount of deposited PEI and PSS increased (Figure 4a). The peaks at 1178, 1124, 1035 and 1007 cm^{-1} are assigned to the asymmetric and symmetric stretching of S=O in PSS.[40] The existence of these peaks verifies the successful deposition of PSS onto the membrane. Raman mapping images offer visible information about the distribution of PEs on the surface, displaying alternating assembly and even dispersion of oppositely charged PEs as illustrated in

Figure S11. The streaming zeta potential became more positive after PEI deposition and more negative after PSS deposition (Figure S12). Moreover, the change of water contact angle followed a similar zig-zag pattern (Figure S13). The PSS-terminated PEM membranes were more hydrophilic than the PEI-terminated PEM membranes, because the negatively charged -SO_3 functional groups tend to form hydrogen bonds with water, leading to a lower water contact angle.[41, 42]

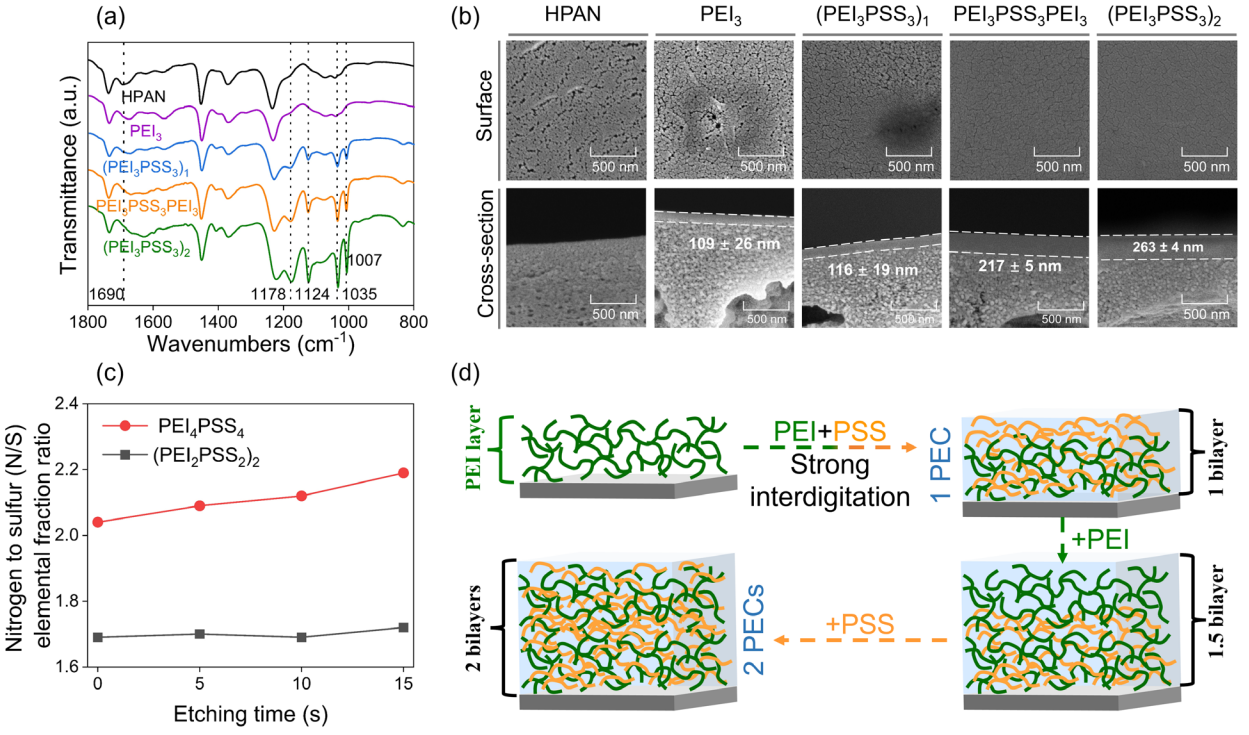

Figure 4. Surface characterization of the $(PEI_nPSS_n)_x$ membranes with different bilayer numbers and scans for each single layer. (a) FTIR spectra, (b) surface and cross-section SEM images, (c) the ratios of elemental fraction of nitrogen (N) to sulfur (S) of the $(PEI_2PSS_2)_2$ and PEI_4PSS_4 membranes determined from the XPS depth profiling analysis, and (d) corresponding schematic of PEM assembly.

345 The top-view FESEM images (Figure 4b) show the morphology of the pristine substrate and the
346 PEM membranes. For the $(PEI_3PSS_3)_1$ membrane, smaller pores can be apparently observed when
347 compared with the HPAN substrate. For the $(PEI_3PSS_3)_2$ membrane, the surface layer became
348 much denser without obvious defects. Furthermore, the $(PEI_3PSS_3)_2$ membrane exhibited a smooth
349 and compact surface (Figure S14). The ultrafine droplets were evenly distributed on the substrate,
350 leading to uniform coverage. Other spray methods such as spray gun and airbrush, generate larger
351 droplets which lead to island-shape deposition on a substrate and cause larger roughness (e.g., Ra
352 is ca. 15 nm).[18]
353 The measurement of the thickness of the PEM from the cross-section SEM images reveals the
354 thickness grows with layering (Figure S15a, b). However, as shown in Figure 4b, the PEI_3 layer
355 has a similar thickness (109 ± 26 nm) to the PEI_3PSS_3 membrane (116 ± 19 nm) and the
356 $PEI_3PSS_3PEI_3$ membrane thickness (217 ± 5 nm) approaches that of the $(PEI_3PSS_3)_2$ membrane
357 (263 ± 4 nm). The data shows that the addition of a PSS layer does not double the thickness of the
358 PEM, but instead, only increases the thickness by ⩽ 20%. Moreover, for the one-bilayer
359 membranes, the thickness growth shows a linear pattern with a rate of ca. 46 nm/scan (Figure S15c,
360 $R^2 = 0.99$), which is about half the combined thickness of the PEI layer plus the PSS layer (88
361 nm/scan, Figure 3c); for the two-bilayer membranes, the thickness exhibits also a linear growth
362 from one to five scans with a rate of ca. 87 nm/scan (Figure S15d, $R^2 = 0.99$), also about half the
363 combined thickness of (PEI+PSS+PEI+PSS) (i.e., 177 nm/scan, Figure 3c). Regardless of the
364 number of scans, the thickness of the two-bilayer membrane is approximately twice that of the
365 one-bilayer membrane (Figure S15). The occurrence of this unique growth pattern is attributed to
366 the interdigitation of PEI and PSS within the PEM structure. We speculate that during the PEM
367 assembly, two adjacent oppositely charged PE layers are strongly interdigitated,[43] forming a

polyelectrolyte complex (PEC) layer instead of a perfect layer-by-layer assembly. This strong interdigitation is likely due to the deep penetration of PSS. The diffusion of PE molecules within the PEM is a widely observed phenomenon.[44-49] For example, Gilbertet al.[48] have used XPS depth profiling to prove the diffusion of chitosan within the PEM of poly(acrylic acid) and poly(ethylene oxide). Taketa et al.[49] have also found that PSS can diffuse within carboxymethyl cellulose/chitosan multilayers through XPS depth profiling.

To explore the internal architectures of the PEM, especially the interdigitation between PEI and PSS, XPS depth profiling was employed to examine the $(PEI_2PSS_2)_2$ and PEI_4PSS_4 membranes, two membranes with theoretically the same material but different assembled structures. The nitrogen (N) and sulfur (S) elements were used to represent the PEI and PSS, respectively, and their N/S atomic ratio was analyzed to evaluate the relative distribution of PEI and PSS within the PEM structure. After optimization, the XPS depth profiling was conducted at the etching time of 5 s, 10 s, 15 s, and 20 s to obtain elemental information at different depths of the PEM's internal structure. The N/S ratios of the $(PEI_2PSS_2)_2$ membrane were consistent at ca. 1.7 from 0 to 15 s (Figure 4c), indicating a uniform distribution of the PEI and PSS components throughout the PEM structure. This observation suggests the formation of a well-intermixed and homogeneous PEC within the $(PEI_2PSS_2)_2$ multilayer. However, for the PEI_4PSS_4 membrane, the N/S ratios increased from 2.0 to 2.2 with increasing etching time from 0 to 15 s (Figure 4c). The increased N/S ratios for the PEI_4PSS_4 membrane suggest a reduced degree of penetration of PSS from the top. This difference is understandable because it is more difficult to well mix two thicker polyelectrolyte layers (i.e., a PEI_4 layer and a PSS_4 layer). At the etching time of 20 s, the N/S ratios of $(PEI_2PSS_2)_2$ and PEI_4PSS_4 membranes increased significantly to 2.7 and 5.0, respectively, indicating the

reaching of the underlying HPAN substrate. In conclusion, the XPS depth profiling analysis confirms the formation of interdigitated PECs as illustrated in Figure 4d.

Membrane Filtration Performance

Water Flux and MWCO. The PE deposition mass increases with more scans, which expectedly increases overall membrane resistance and decreases PWP (Figure 5a). The HPAN substrate had a PWP of 208.8 ± 21.4 L m^{-2} h^{-1} bar^{-1}. When the PEI layer was the terminal layer, the PWP did not decrease with increased scans, because the PEI layer did not exert significant resistance to water transport due to its swelling in water.[50, 51] Following subsequent PSS and PEI alternative deposition, the PWP decreased as the bilayer number increased (Figure 5a). The PWP decreased from 12.0 ± 0.8 L m^{-2} h^{-1} bar^{-1} (one-bilayer membranes) to 5.4 ± 1.3 L m^{-2} h^{-1} bar^{-1} (two-bilayer membranes) under three scans condition. For the two-bilayer membranes, the PWP of PEM membranes decreased from 13.3 to 3.3 L m^{-2} h^{-1} bar^{-1} when the scan number increased from one to five. The PWP reduction is attributed to the effective barrier generated by the interdigitated PEI and PSS chains on the substrate surface.[52] This is in accordance with the fact that the thickness of the layers increases with more bilayers (Figure 4b), thereby engendering higher overall hydraulic resistance.

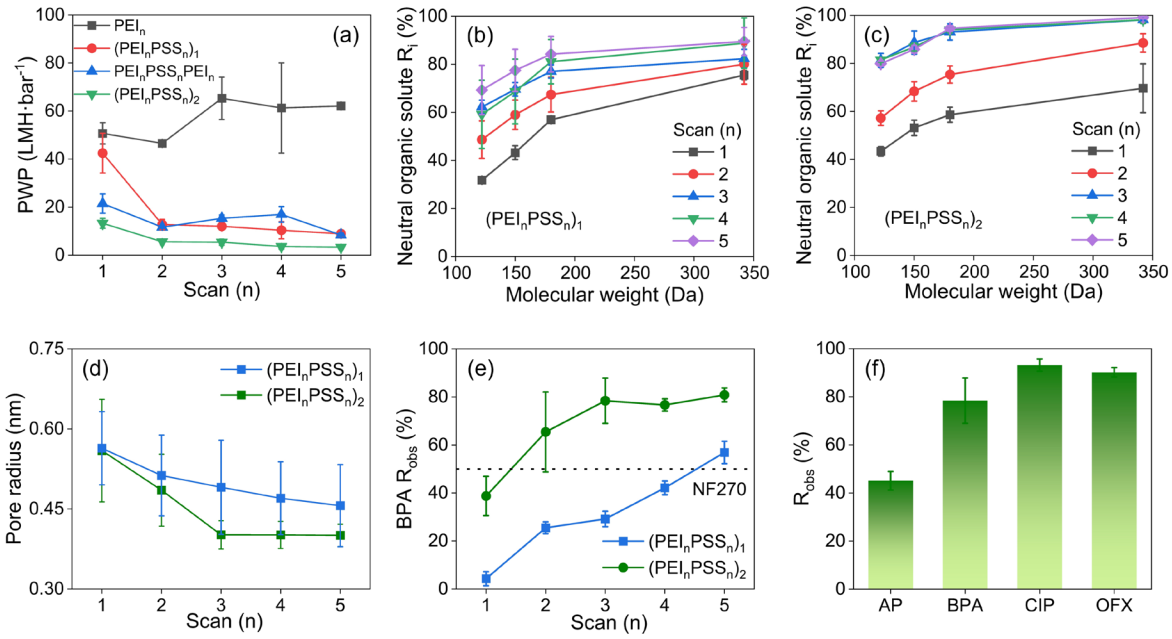

407

408 **Figure 5**. Filtration performance and pore characteristics of the $(PEI_nPSS_n)_x$ membranes with
409 different bilayer numbers and scans: (a) PWP, (b) intrinsic rejection (R_i) of neutral organic solutes
410 by the one-bilayer $(PEI_nPSS_n)_1$ membranes, (c) intrinsic rejection (R_i) of neutral organic solutes by
411 the two-bilayer $(PEI_nPSS_n)_2$ membranes, (d) estimated mean pore radius, (e) observed rejection of
412 BPA (BPA R_{obs}), and (f) observed rejection (R_{obs}) of AP, BPA, CIP, and OFX by the $(PEI_3PSS_3)_2$
413 membrane.

414 Moreover, the observed rejections (R_{obs}) of neutral organic compounds of increasing molecular
415 weights were evaluated (Figure S16a, b), and the intrinsic rejections were calculated based on the
416 experimentally obtained mass transfer coefficients (details in Text S4, and data in Table S2).[25] The
417 MWCO values were determined from the rejection curves as the molecular weight corresponding
418 to a 90% rejection, and the intrinsic rejections were fitted by the steric hindrance pore model to
419 obtain the pore size of the PEM membranes (Text S5).[26, 27] The pore sizes estimated from the test
420 of each organic solute were averaged to obtain the pore size for each membrane.[27, 53] Overall, the

MWCO of the PEM membranes decreased with the increase of scan numbers and the MWCO of all the one-bilayer membranes was larger than 342 Da (Figure 5b, c). As the scan number increased from one to five, the corresponding mean pore radii of the one-bilayer membranes decreased from 0.56 to 0.46 nm (Figure 5d). As the scan number increased from one to three, the mean pore radii of the two-bilayer membranes decreased from 0.56 to 0.40 nm (Figure 5d), which falls within the range for nanofiltration membranes.[54] There was little difference among $(PEI_3PSS_3)_2$, $(PEI_4PSS_4)_2$, and $(PEI_5PSS_5)_2$, whose average pore radii were ca. 0.40 nm. The two-bilayer membranes had a smaller pore radius than the one-bilayer membranes when the scan number was the same (n=2-5), except in the case of one scan (Figure 5d). This was likely due to too few PE materials deposited under one scan, which did not form a selective PE layer. The observed trend of decreasing PWP with increasing bilayer number can be attributed to the smaller pore radius and increased thickness of the PEM with repeated LbL deposition cycles.

The Na_2SO_4 rejection of the one-bilayer membranes increased from 16% to 55% when the printing scan increased from one to five (Figure S17a). The Na_2SO_4 rejection of the two-bilayer membranes ranged from 47% to 58%. The respective hydration radii of 0.36 and 0.38 nm for Na^+ and SO_4^{2-} [55] are smaller than the smallest pore radius (0.40 nm) of all the PEM membranes in our study. The Na_2SO_4 rejection by the resultant PEM membranes is predominantly governed by electrostatic repulsion. We further evaluated the rejection of various salts by the $(PEI_3PSS_3)_2$ membrane, and the results further confirmed the significant role of electrostatic interactions in ion rejection. The NaCl rejection was 22%, the rejections of Na_2SO_4 and $MgSO_4$ were 58% and 34%, respectively, and the $MgCl_2$ rejection was 13% (Figure S17b). As the $(PEI_3PSS_3)_2$ membranes are negatively charged, they are effective in rejecting salts with divalent anions. The negatively

443 charged top PSS layer of the PEM membranes facilitates the transport of Mg^{2+} ions, resulting in a
444 low rejection of $MgCl_2$.

445 The one-bilayer PEM membranes can effectively retain pollutants with large molecular weight
446 like humic acid (> 90% rejection regardless of the scan numbers, Figure S19) while maintaining
447 high water permeability. The two-bilayer PEM membrane can remove various types of
448 micropollutants. Furthermore, in the long-term filtration process lasting 96 h, the $(PEI_3PSS_3)_2$
449 membrane maintained a steady state in terms of pure water permeability and the rejection of
450 glucose and Na_2SO_4 (Figure S19). The above results show that the filtration performance and mean
451 pore radius of the PEM membranes can be tailored by simultaneously tuning the scan and bilayer
452 numbers.

453 ***Retention of Micropollutants.*** As the scan number increased from one to five, the BPA rejection
454 of the one-bilayer membranes increased from 12.7 % to 67.9% (Figure 5e). Furthermore, the
455 enhanced rejection performance with increased bilayer number was more obvious than with
456 increased scans. As for the two-bilayer membranes, the BPA rejection increased from 38.7% to
457 80.8% with scans increasing from one to five. The highest BPA rejection of the two-bilayer
458 membranes was 80.8%, which is superior to that of the commercial NF270 membranes (ca.
459 40%).[56, 57] To elucidate the mechanisms underlying the enhanced BPA rejection, we also
460 conducted similar experiments to obtain the mass transfer coefficient of the NF270 membrane and
461 its intrinsic rejections of neutral solutes. The MWCO of NF270 was ca. 290 Da based on observed
462 rejections of these sugars, which is consistent with the literature values.[58, 59] Based on intrinsic
463 rejections, its MWCO was ca. 160 Da (Figure S16c), which was similar to that of the $(PEI_3PSS_3)_2$
464 membrane. However, the intrinsic rejection of BPA by the $(PEI_3PSS_3)_2$ membrane was still higher
465 than that by the NF270 membranes (Figure S20), which suggests size exclusion is not the only

466 factor determining its rejection. Since the charge of BPA is neutral at pH 7 (pK_{a1} = 9.6, and pK_{a2}
467 = 10.2),[60] the electrostatic repulsion effect is considered negligible in this case. Therefore, the
468 lower rejection of BPA by the NF 270 membrane is likely because that the rates of sorption and
469 transmission of BPA across a (more) hydrophobic NF270 membrane are considerably increased
470 by hydrophobic interactions.[61]

471 We further evaluated the rejection of the AP (188 $g \cdot mol^{-1}$), BPA (228 $g \cdot mol^{-1}$), CIP (331 $g \cdot mol^{-1}$), OFX (361 $g \cdot mol^{-1}$) by the $(PEI_3PSS_3)_2$ membrane. The rejection trend of these four micropollutants followed the size exclusion mechanism in accordance with the MWCO (294 $g \cdot mol^{-1}$ based on observed rejections) of the membrane. As shown in Figure 5f, only 45.1% of AP was retained, while CIP and OFX exhibited rejection exceeding 90%. This high rejection of CIP and OFX demonstrates the $(PEI_3PSS_3)_2$ membrane to be defect-free.

477 **Environmental Implications**

478 Our AAP method has the advantage of low time and material consumption compared to the
479 conventional dip coating. For example, the $(PEI_3PSS_3)_2$ membrane with an area of 64.8 cm^2 was
480 fabricated using only 18 min (Text S1) and 6 mL of the PE solution. And the fabrication time can
481 be further decreased by using more spray nozzles. In contrast, using dip-coating to obtain a two-
482 bilayer PEM membrane requires a minimum of several hours and hundreds of milliliters of
483 solution.[50, 62, 63] The rapid, controlled, and efficient deposition of polyelectrolytes is a key
484 advantage of our AAP method, making it promising for various applications requiring thin,
485 uniform coatings. The obtained membranes have comparable structure and separation performance
486 to those obtained via dip coating. Ranging from loose to dense nanofiltration, these membranes
487 are well-suited for various water treatment applications, from micropollutant removal to humic
488 acid filtration.

Future efforts can be devoted to adjusting the PEM structure to achieve the synergistic control of pore and charge properties. The current PEM membranes exhibit a mild negative charge and thus a moderate Na_2SO_4 rejection of ca. 60% (Figure S17), due to low PSS deposition. By adjusting the composition and layering of PEs, the desirable separation of charged ions can be obtained. Furthermore, incorporating additives into the PE solutions allows additional functionalities and further improvement of membrane properties (e.g., permeability, selectivity, stability, and chlorine resistance). Lastly, the AAP method enables the deposition of PE and other materials onto complex geometries, including three-dimensional structures. This capability opens up possibilities for manufacturing membranes with intricate designs.

SUPPORTING INFORMATION

The Supporting Information is available free of charge at XX.

Description of the aerosol-assisted printing method, aerosol deposition characterization, chemical analysis, concentration polarization analysis, membrane pore size analysis, and PE layer growth analysis; data of thickness and mass transfer coefficients of different PEM membranes; aerosol deposition data including velocity distribution field, droplet size distribution, deposition efficiency; and characterization of the PEM membranes (TEM, SEM and AFM images, Raman mapping images, surface zeta potential, and water contact angle).

ACKNOWLEGEMENTS

This work was supported by Hong Kong Research Grants Council's General Research Fund Scheme (15214222) and Science, Technology and Innovation Commission of Shenzhen Municipality (SGDX20210823103401009).

REFERENCES

(1) Durmaz, E. N.; Sahin, S.; Virga, E.; de Beer, S.; de Smet, L. C. P. M.; de Vos, W. M. Polyelectrolytes as building blocks for next-generation membranes with advanced functionalities. *ACS Appl. Polym. Mater.* **2021**, *3* (9), 4347-4374. DOI: 10.1021/acsapm.1c00654.

(2) Li, Q.; Zhang, N.; Li, Z.; Gao, Z.; Yan, T.; Qian, Z.; Xu, S.; Wang, J. Brush assisted layer-by-layer assembled lignin/polyelectrolyte membrane. *Mater. Lett.* **2021**, *292*, 129650. DOI: 10.1016/j.matlet.2021.129650.

(3) Brinke, E. t.; Reurink, D. M.; Achterhuis, I.; de Grooth, J.; de Vos, W. M. Asymmetric polyelectrolyte multilayer membranes with ultrathin separation layers for highly efficient micropollutant removal. *Appl. Mater. Today* **2020**, *18*, 100471. DOI: 10.1016/j.apmt.2019.100471.

(4) de Grooth, J.; Haakmeester, B.; Wever, C.; Potreck, J.; de Vos, W. M.; Nijmeijer, K. Long term physical and chemical stability of polyelectrolyte multilayer membranes. *J. Membr. Sci.* **2015**, *489*, 153-159. DOI: 10.1016/j.memsci.2015.04.031.

(5) Cho, K. L.; Hill, A. J.; Caruso, F.; Kentish, S. E. Chlorine resistant glutaraldehyde crosslinked polyelectrolyte multilayer membranes for desalination. *Adv. Mater.* **2015**, *27* (17), 2791-2796. DOI: 10.1002/adma.201405783.

(6) Elshof, M. G.; de Vos, W. M.; de Grooth, J.; Benes, N. E. On the long-term pH stability of polyelectrolyte multilayer nanofiltration membranes. *J. Membr. Sci.* **2020**, *615*, 118532. DOI: 10.1016/j.memsci.2020.118532.

(7) Ba, C.; Ladner, D. A.; Economy, J. Using polyelectrolyte coatings to improve fouling resistance of a positively charged nanofiltration membrane. *J. Membr. Sci.* **2010**, *347* (1-2), 250-259. DOI: 10.1016/j.memsci.2009.10.031.

(8) Sanyal, O.; Liu, Z.; Meharg, B. M.; Liao, W.; Lee, I. Development of polyelectrolyte multilayer membranes to reduce the COD level of electrocoagulation treated high-strength wastewater. *J. Membr. Sci.* **2015**, *496*, 259-266. DOI: 10.1016/j.memsci.2015.09.011.

(9) Son, M.; Yang, W.; Bucs, S. S.; Nava-Ocampo, M. F.; Vrouwenvelder, J. S.; Logan, B. E. Polyelectrolyte-based sacrificial protective layer for fouling control in reverse osmosis desalination. *Environ. Sci. Technol. Lett.* **2018**, *5* (9), 584-590. DOI: 10.1021/acs.estlett.8b00400.

(10) Liang, Y.; Lin, S. Intercalation of zwitterionic surfactants dramatically enhances the performance of low-pressure nanofiltration membrane. *J. Membr. Sci.* **2020**, *596*, 117726. DOI: 10.1016/j.memsci.2019.117726.

(11) Li, X.; Liu, C.; Van der Bruggen, B. Polyelectrolytes self-assembly: Versatile membrane fabrication strategy. *J. Mater. Chem. A* **2020**, *8* (40), 20870-20896. DOI: 10.1039/d0ta07154d.

(12) Ma, D.; Li, H.; Meng, Z.; Zhang, C.; Zhou, J.; Xia, J.; Wang, Y. Absolute and fast removal of viruses and bacteria from water by spraying-assembled carbon-nanotube membranes. *Environ. Sci. Technol.* **2021**, *55* (22), 15206-15214. DOI: 10.1021/acs.est.1c04644.

(13) Zhao, G. J.; Han, W. J.; Dong, L. L.; Fan, H. W.; Qu, Z.; Gu, J. H.; Meng, H. Sprayed separation membranes: A systematic review and prospective opportunities. *Green Energy Environ.* **2022**, *7* (6), 1143-1160. DOI: 10.1016/j.gee.2022.04.001.

(14) Schlenoff, J. B.; Dubas, S. T.; Farhat, T. Sprayed polyelectrolyte multilayers. *Langmuir* **2000**, *16* (26), 9968-9969. DOI: 10.1021/la001312i.

(15) Cho, K. L.; Lomas, H.; Hill, A. J.; Caruso, F.; Kentish, S. E. Spray assembled, cross-linked polyelectrolyte multilayer membranes for salt removal. *Langmuir* **2014**, *30* (29), 8784-8790. DOI: 10.1021/la501855k.

(16) Li, Q.; Chen, G. Q.; Liu, L.; Kentish, S. E. Spray assisted layer-by-layer assembled one-bilayer polyelectrolyte reverse osmosis membranes. *J. Membr. Sci.* **2018**, *564*, 501-507. DOI: 10.1016/j.memsci.2018.07.047.

(17) Felton, L. A. Mechanisms of polymeric film formation. *Int. J. Pharm.* **2013**, *457* (2), 423-427. DOI: 10.1016/j.ijpharm.2012.12.027.

(18) Xiang, F.; Givens, T. M.; Grunlan, J. C. Fast spray deposition of super gas barrier polyelectrolyte multilayer thin films. *Ind. Eng. Chem. Res.* **2015**, *54* (19), 5254-5260. DOI: 10.1021/acs.iecr.5b01367.

(19) Bose, S.; Keller, S. S.; Alstrøm, T. S.; Boisen, A.; Almdal, K. Process optimization of ultrasonic spray coating of polymer films. *Langmuir* **2013**, *29* (23), 6911-6919. DOI: 10.1021/la4010246.

(20) Yunker, P. J.; Still, T.; Lohr, M. A.; Yodh, A. G. Suppression of the coffee-ring effect by shape-dependent capillary interactions. *Nature* **2011**, *476* (7360), 308-311. DOI: 10.1038/nature10344.

(21) Hart, M. B.; Scotto, C. S.; Tucker, J. E.; McPherson, D. C.; Minter, Z.; Kesavan, J.; Silcott, D.; Lin, H. B.; Eversole, J. D. Toward biological aerosol reference standards. *Aerosol Sci. Technol.* **2020**, *54* (5), 601-610. DOI: 10.1080/02786826.2019.1708860.

(22) Wang, W. N.; Jiang, Y.; Biswas, P. Evaporation-induced crumpling of graphene oxide nanosheets in aerosolized droplets: Confinement force relationship. *J. Phys. Chem. Lett.* **2012**, *3* (21), 3228-3233. DOI: 10.1021/jz3015869.

(23) May, K. R. The collison nebulizer: Description, performance and application. *J. Aerosol Sci.* **1973**, *4* (3), 235-243. DOI: 10.1016/0021-8502(73)90006-2.

578 (24) Jiang, Y.; Wang, W.-N.; Biswas, P.; Fortner, J. D. Facile aerosol synthesis and
579 characterization of ternary crumpled graphene-TiO2-magnetite nanocomposites for advanced
580 water treatment. *ACS Appl. Mater. Interfaces.* **2014**, *6* (14), 11766-11774. DOI:
581 10.1021/am5025275.
582 (25) Bason, S.; Kaufman, Y.; Freger, V. Analysis of ion transport in nanofiltration using
583 phenomenological coefficients and structural characteristics. *J. Phys. Chem. B* **2010**, *114* (10),
584 3510-3517. DOI: 10.1021/jp911615n.
585 (26) DuChanois, R. M.; Epsztein, R.; Trivedi, J. A.; Elimelech, M. Controlling pore structure
586 of polyelectrolyte multilayer nanofiltration membranes by tuning polyelectrolyte-salt interactions.
587 *J. Membr. Sci.* **2019**, *581*, 413-420. DOI: 10.1016/j.memsci.2019.03.077.
588 (27) Boo, C.; Wang, Y. K.; Zucker, I.; Choo, Y.; Osuji, C. O.; Elimelech, M. High performance
589 nanofiltration membrane for effective removal of perfluoroalkyl substances at high water recovery.
590 *Environ. Sci. Technol.* **2018**, *52* (13), 7279-7288. DOI: 10.1021/acs.est.8b01040.
591 (28) Bigioni, T. P.; Lin, X.-M.; Nguyen, T. T.; Corwin, E. I.; Witten, T. A.; Jaeger, H. M.
592 Kinetically driven self assembly of highly ordered nanoparticle monolayers. *Nat. Mater* **2006**, *5*
593 (4), 265-270. DOI: 10.1038/nmat1611.
594 (29) Modi, S.; Foston, M. B.; Biswas, P. Controlled synthesis of smaller than 100 nm lignin
595 nanoparticles in a furnace aerosol reactor. *ACS ES&T Engineering* **2023**, *3* (5), 671-681. DOI:
596 10.1021/acsestengg.2c00386.
597 (30) Chen, G.; Gu, Y.; Tsang, H.; Hines, D. R.; Das, S. The effect of droplet sizes on overspray
598 in aerosol‐jet printing. *Adv. Eng. Mater.* **2018**, *20* (8), 1701084. DOI: 10.1002/adem.201701084
599 (acccessed 2024/01/07).

(31) Hinds, W. C. *Aerosol technology : properties, behavior, and measurement of airborne particles*; Wiley, 1999.

(32) Friedlander, S. K.; Smoke, D. Haze: Fundamentals of aerosol dynamics. Oxford University Press, New York: 2000.

(33) Wang, W. N.; Widiyastuti, W.; Lenggoro, I. W.; Kim, T. O.; Okuyama, K. Photoluminescence optimization of luminescent nanocomposites fabricated by spray pyrolysis of a colloid-solution precursor. *J. Electrochem. Soc.* **2007**, *154* (4), J121-J128. DOI: 10.1149/1.2435698.

(34) Wang, W. N.; Kaihatsu, Y.; Iskandar, F.; Okuyama, K. Highly luminous hollow chloroapatite phosphors formed by a template-free aerosol route for solid-state lighting. *Chem. Mater.* **2009**, *21* (19), 4685-4691. DOI: 10.1021/cm9018327.

(35) Haynie, D. T.; Cho, E.; Waduge, P. "In and out diffusion" hypothesis of exponential multilayer film buildup revisited. *Langmuir* **2011**, *27* (9), 5700-5704. DOI: 10.1021/la104516a.

(36) Porcel, C. H.; Izquierdo, A.; Ball, V.; Decher, G.; Voegel, J. C.; Schaaf, P. Ultrathin coatings and (poly (glutamic acid)/polyallylamine) films deposited by continuous and simultaneous spraying. *Langmuir* **2005**, *21* (2), 800-802. DOI: 10.1021/la047570n.

(37) Azinfar, A.; Neuber, S.; Vancova, M.; Sterba, J.; Stranak, V.; Helm, C. A. Self-patterning polyelectrolyte multilayer films: Influence of deposition steps and drying in a vacuum. *Langmuir* **2021**, *37* (35), 10490-10498. DOI: 10.1021/acs.langmuir.1c01409.

(38) Cranston, E. D.; Gray, D. G. Morphological and optical characterization of polyelectrolyte multilayers incorporating nanocrystalline cellulose. *Biomacromolecules* **2006**, *7* (9), 2522-2530. DOI: 10.1021/bm0602886.

(39) Zhao, S.; Wang, Z. A loose nano-filtration membrane prepared by coating HPAN UF membrane with modified PEI for dye reuse and desalination. *J. Membr. Sci.* **2017**, *524*, 214-224. DOI: 10.1016/j.memsci.2016.11.035.

(40) Alemu, D.; Wei, H. Y.; Ho, K. C.; Chu, C. W. Highly conductive PEDOT: PSS electrode by simple film treatment with methanol for ITO-free polymer solar cells. *Energy Environ. Sci.* **2012**, *5* (11), 9662-9671, 10.1039/C2EE22595F. DOI: 10.1039/c2ee22595f.

(41) Liu, C.; Shi, L.; Wang, R. Crosslinked layer-by-layer polyelectrolyte nanofiltration hollow fiber membrane for low-pressure water softening with the presence of SO42− in feed water. *J. Membr. Sci.* **2015**, *486*, 169-176. DOI: 10.1016/j.memsci.2015.03.050.

(42) Qi, S.; Li, W.; Zhao, Y.; Ma, N.; Wei, J.; Chin, T. W.; Tang, C. Y. Influence of the properties of layer-by-layer active layers on forward osmosis performance. *J. Membr. Sci.* **2012**, *423-424*, 536-542. DOI: 10.1016/j.memsci.2012.09.009.

(43) Castelnovo, M.; Joanny, J.-F. Formation of polyelectrolyte multilayers. *Langmuir* **2000**, *16* (19), 7524-7532. DOI: 10.1021/la000211h.

(44) Picart, C.; Mutterer, J.; Richert, L.; Luo, Y.; Prestwich, G. D.; Schaaf, P.; Voegel, J. C.; Lavalle, P. Molecular basis for the explanation of the exponential growth of polyelectrolyte multilayers. *Proc. Natl. Acad. Sci. U.S.A.* **2002**, *99* (20), 12531-12535. DOI: 10.1073/pnas.202486099 (acccessed 2024/04/23).

(45) Zacharia, N. S.; Modestino, M.; Hammond, P. T. Factors influencing the interdiffusion of weak polycations in multilayers. *Macromolecules* **2007**, *40* (26), 9523-9528. DOI: 10.1021/ma071828+.

643 (46) Sill, A.; Nestler, P.; Thran, P.; Helm, C. A. Dependence of PSS diffusion in multilayers of
644 entangled PDADMA on temperature and salt concentration: More than one diffusion constant.
645 *Macromolecules* **2021**, *54* (20), 9372-9384. DOI: 10.1021/acs.macromol.1c00639.
646 (47) Sill, A.; Nestler, P.; Azinfar, A.; Helm, C. A. Tailorable polyanion diffusion coefficient in
647 LbL films: The role of polycation molecular weight and polymer conformation. *Macromolecules*
648 **2019**, *52* (22), 9045-9052. DOI: 10.1021/acs.macromol.9b01761.
649 (48) Gilbert, J. B.; Rubner, M. F.; Cohen, R. E. Depth-profiling X-ray photoelectron
650 spectroscopy (XPS) analysis of interlayer diffusion in polyelectrolyte multilayers. *Proc. Natl.*
651 *Acad. Sci. U.S.A.* **2013**, *110* (17), 6651-6656. DOI: 10.1073/pnas.1222325110 (acccessed
652 2024/08/06).
653 (49) Taketa, T. B.; Rocha Neto, J. B. M.; dos Santos, D. M.; Fiamingo, A.; Beppu, M. M.;
654 Campana-Filho, S. P.; Cohen, R. E.; Rubner, M. F. Tracking sulfonated polystyrene diffusion in a
655 chitosan/carboxymethyl cellulose layer-by-layer film: exploring the internal architecture of
656 nanocoatings. *Langmuir* **2020**, *36* (18), 4985-4994. DOI: 10.1021/acs.langmuir.0c00544.
657 (50) Scheepers, D.; de Keizer, J.; Borneman, Z.; Nijmeijer, K. The pH as a tool to tailor the
658 performance of symmetric and asymmetric layer-by-layer nanofiltration membranes. *J. Membr.*
659 *Sci.* **2023**, *670*, 121320. DOI: 10.1016/j.memsci.2022.121320.
660 (51) Zhu, Q.; Shentu, B.; Liu, Q.; Weng, Z. Swelling behavior of polyethylenimine-cobalt
661 complex in water. *Eur. Polym. J.* **2006**, *42* (6), 1417-1422. DOI: 10.1016/j.eurpolymj.2005.12.004.
662 (52) Ng, L. Y.; Mohammad, A. W.; Ng, C. Y. A review on nanofiltration membrane fabrication
663 and modification using polyelectrolytes: Effective ways to develop membrane selective barriers
664 and rejection capability. *Adv. Colloid Interface Sci.* **2013**, *197-198*, 85-107. DOI:
665 10.1016/j.cis.2013.04.004.

(53) Dang, H. Q.; Price, W. E.; Nghiem, L. D. The effects of feed solution temperature on pore size and trace organic contaminant rejection by the nanofiltration membrane NF270. *Sep. Purif. Technol.* **2014**, *125*, 43-51. DOI: https://doi.org/10.1016/j.seppur.2013.12.043.

(54) Zhao, Y.; Tong, T.; Wang, X.; Lin, S.; Reid, E. M.; Chen, Y. Differentiating solutes with precise nanofiltration for next generation environmental separations: a review. *Environ. Sci. Technol.* **2021**, *55* (3), 1359-1376. DOI: 10.1021/acs.est.0c04593.

(55) Liang, Y.; Zhu, Y.; Liu, C.; Lee, K. R.; Hung, W. S.; Wang, Z.; Li, Y.; Elimelech, M.; Jin, J.; Lin, S. Polyamide nanofiltration membrane with highly uniform sub-nanometre pores for sub-1 A precision separation. *Nat Commun* **2020**, *11* (1), 2015. DOI: 10.1038/s41467-020-15771-2.

(56) Zhang, H.; Zhang, H.; Luo, J.; Wan, Y. Enzymatic cascade catalysis in a nanofiltration membrane: Engineering the microenvironment by synergism of separation and reaction. *ACS Appl. Mater. Interfaces.* **2019**, *11* (25), 22419-22428. DOI: 10.1021/acsami.9b05371.

(57) Yuksel, S.; Kabay, N.; Yuksel, M. Removal of bisphenol A (BPA) from water by various nanofiltration (NF) and reverse osmosis (RO) membranes. *J. Hazard. Mater.* **2013**, *263 Pt 2*, 307-310. DOI: 10.1016/j.jhazmat.2013.05.020.

(58) Gao, Y.; Wang, K.; Wang, X.-m.; Huang, X. Exploitation of Amine Groups Cooped up in Polyamide Nanofiltration Membranes to Achieve High Rejection of Micropollutants and High Permeance of Divalent Cations. *Environ. Sci. Technol.* **2022**, *56* (15), 10954-10962. DOI: 10.1021/acs.est.2c02410.

(59) Wang, K.; Fu, W.; Wang, X.-m.; Xu, C.; Gao, Y.; Liu, Y.; Zhang, X.; Huang, X. Molecular Design of the Polyamide Layer Structure of Nanofiltration Membranes by Sacrificing Hydrolyzable Groups toward Enhanced Separation Performance. *Environ. Sci. Technol.* **2022**, *56* (24), 17955-17964. DOI: 10.1021/acs.est.2c04232.

689 (60) Choi, Y. J.; Lee, L. S. Partitioning behavior of bisphenol alternatives BPS and BPAF
690 compared to BPA. *Environ. Sci. Technol.* **2017**, *51* (7), 3725-3732. DOI: 10.1021/acs.est.6b05902.
691 (61) Guo, H.; Deng, Y.; Tao, Z.; Yao, Z.; Wang, J.; Lin, C.; Zhang, T.; Zhu, B.; Tang, C. Y.
692 Does hydrophilic polydopamine coating enhance membrane rejection of hydrophobic endocrine-
693 disrupting compounds? *Environ. Sci. Technol. Lett.* **2016**, *3* (9), 332-338. DOI:
694 10.1021/acs.estlett.6b00263.
695 (62) Gopalakrishnan, A.; Janardhanan, D. V.; Sasi, S.; Aravindakumar, C. T.; Aravind, U. K.
696 Organic micropollutant removal and phosphate recovery by polyelectrolyte multilayer membranes:
697 Impact of buildup interactions. *Chemosphere* **2024**, *350*, 141078. DOI:
698 10.1016/j.chemosphere.2023.141078.
699 (63) Liang, Y.; Lin, S. Mechanism of permselectivity enhancement in polyelectrolyte-dense
700 nanofiltration membranes via surfactant-assembly intercalation. *Environ. Sci. Technol.* **2021**, *55*
701 (1), 738-748. DOI: 10.1021/acs.est.0c06866.

702